Dynamic Response of Buck Converter With Auxiliary Current Control: Analysis and Design of Practical Implementation

Dongwook Kim and Jong-Won Shin, *Member, IEEE*

***Abstract*—An in-depth analysis on the load transient operation of a buck converter with auxiliary current control is presented in this article. The analysis quantifies the effects of nonideal characteristics, such as the equivalent series resistance, inductor current and output voltage ripples, time delay, and slew rate of the load current, on the fluctuation of the output voltage in a practical implementation. The analysis results reveals that some of the non-idealities may cancel each other out and become negligible in the implementation. A design considering the nonidealities can achieve the transient-wise capacitor charge balance of the output capacitor and minimize the output voltage deviation during the load transient. The agreement between the simulation and experimental results validates the effectiveness and precision of the proposed analysis and design.**

***Index Terms*—Auxiliary current control, buck converter, capacitor charge balance, load transient response.**

I. Introduction

THE DYNAMIC response during a load transient is one of the most important performance factors of general dc–dc converters. Applications, such as point-of-load (POL) power conversion, avionics and spacecraft power systems, and power supplies for medical instruments require tight regulation of the output voltage. Various control techniques and topologies have been proposed to improve the dynamic response and minimize the output voltage fluctuation of buck converters. The load transient response by the peak-current-controlled duty ratio [1] has been analyzed with consideration to the parasitic resistances of the buck converter. Adaptive on-time control [2] reduces both the output voltage deviation and the inductor current.

Control techniques that do not predict the load current focus on the cycle-by-cycle capacitor-charge-balance (CCB) of the output capacitor to enhance the dynamic performance [3]–[8]. The time-optimal control (TOC) [3], [4] minimizes the output voltage deviation through a single switching with an extended period during the load transient. The response of the TOC has been compared to the load line regulation [5], which suggests that the maximum undershoot and overshoot are identical whether the CCB is satisfied. However, a large steady-state error occurs in the TOC if the CCB is not precisely satisfied. The TOC has been analyzed with additional precision by including the transition detection delay of an integrated circuit (IC) used in practical applications [6], [7], equivalent series resistance (ESR), and the inductor current and output voltage ripples of the main converter [7]. An auxiliary inductor with bidirectional switches [8] achieves the CCB in each switching cycle with consideration to the time delay, while the auxiliary circuit undergoes voltage and current stress owing to the discharged energy in the auxiliary inductor.

Other control strategies [9]–[21] have achieved a transient-wise CCB. The influence of the inductor current and output voltage ripples has been addressed in [9], [10] to mitigate the dynamic response error. The output voltage fluctuation by the time delay, such as the propagation delay of analog ICs and the latency in digital ICs, has been discussed in [11]–[18]. Resistive auxiliary circuits [11] have shown that the maximum undershoot or overshoot varies depending on the configuration of the auxiliary circuit and its transition detection delay. A concept presented in [12] and [13] controls the average current of the auxiliary inductor to enhance the unloading transient response by taking ESR into account. The single- or two-phase [14] and four-phase buck converter [15] have been used to reflect the ESR of the output capacitor and time delay for the purpose of resolving the mismatched CCB. The work in [16]–[18] have used resonance and soft switching, which attenuates the switching loss of the auxiliary circuit and electromagnetic interference. The first undershoot or overshoot may be smaller than the subsequent voltage error owing to the charge time of the resonant capacitor, described in [16]. Peak-controlled auxiliary current in critical conduction mode (CRM) [17], [18] suppresses the output voltage deviation with high-efficiency soft-switching auxiliary converter. The fact that the auxiliary converter is bidirectional implies that the proposed control technique is also applicable to general bidirectional converters.

The slew rate of the transient load current has been investigated by several studies. The limited slew rate of the load current discussed in [10] and [19]–[21] attenuates the output

Manuscript received March 4, 2021; revised May 4, 2021; accepted June 2, 2021. Date of publication June 8, 2021; date of current version August 16, 2021. This work was supported by the National Research Foundation of Korea through Energy Cloud R&D Program funded by the Ministry of Science and ICT under Grant 2019M3F2A1073313 and Basic Science Research Program funded by the Ministry of Education under Grant NRF-2018R1D1A1B07050968. Recommended for publication by Associate Editor C.N.M. Ho. *(Corresponding author: Jong-Won Shin.)*

The authors are with the School of Energy Systems Engineering, Chung-Ang University, Seoul 06974, South Korea (e-mail: kimdu95@cau.ac.kr; jwshin@cau.ac.kr).

Color versions of one or more figures in this article are available at https://doi.org/10.1109/TPEL.2021.3087607.

Digital Object Identifier 10.1109/TPEL.2021.3087607

voltage fluctuation and thus enables a reduction in the size of the inductor and capacitor. A multiphase buck converter with an output impedance sensor [19] minimizes the parasitic components of the output capacitor and achieves a high slew rate for the load current. Pre-energized auxiliary circuits [20] for fast load variation have been implemented to alleviate the effect of the slew rate. A buck converter with a coupled inductor [21] with various capacitors, such as an electrolytic capacitor, organic semiconductor condenser, and ceramic capacitor, has been considered to compare the slew rate of the load current.

The peak-controlled auxiliary current in CRM [17], [18] improves the output voltage regulation of the buck converter during the load transient. However, output voltage error due to the non-ideal characteristics in practical implementation was not analyzed thoroughly. Theoretically designed amplifier gains of the current sensing circuitry in the prototype hardware required additional adjustments to minimize the error and complete the transient-wise CCB.

This article presents an in-depth analysis on how the non-idealities in practical implementations affect the output voltage during the step-up load transient. The non-idealities include the ESR of the output capacitor, ripples of inductor current and output voltage, time delay, and slew rate of the load current. The analysis presented herein is accurate and useful for estimating the load transient response in applications, such as POL converters, wherein abrupt load variation frequently occurs and the dynamic performance is crucial.

The remainder of this article is organized as follows. Section II reviews the concept of the peak-controlled auxiliary current in CRM. Section III analyzes the effect of the ESR, inductor current and output voltage ripples, time delay, and slew rate of the load current on the dynamic response. The analysis results are compared to results obtained by simulation, and the validity of the analysis is demonstrated by the fact that the experimental waveforms are in good agreement with the simulation results, which are discussed in Section IV. The conclusion drawn from this article is discussed in Section V.

II. Review of Auxiliary Current Control in Ideal Implementation

The control technique in [17], [18] utilizes the transient-wise CCB to minimize the output voltage deviation. Fig. 1(a) illustrates the main buck converter (Q_1, Q_2, and L_1) and auxiliary buck/boost converter (Q_3, Q_4, and L_2) sharing an output capacitor C_O. The auxiliary converter functions as a buck converter when the load current steps up and emulates a boost converter when the load steps down. The voltages v_{gsi}, V_{in}, and v_O represent the gate-source voltage of the MOSFET Q_i ($i = 1, 2, 3,$ or 4), input voltage, and output voltage, respectively. Currents i_{L1} and i_{L2} flow through L_1 and L_2. Currents i_{O1} and i_{O2} are the load currents before and after the transient, respectively. The control circuit is realized using five functional blocks, as shown in Fig. 1(b): voltage mode control, generating envelope, detecting load transition, on/off control of Q_3 or Q_4, and signal router and gate driver. During the load transient, $v_{\mathrm{gs}\,1}$–$v_{\mathrm{gs}\,4}$ are controlled by the auxiliary current control block. In the steady-state, Q_1 and Q_2 are operated by the voltage mode control block, whereas Q_3 and Q_4 are kept OFF.

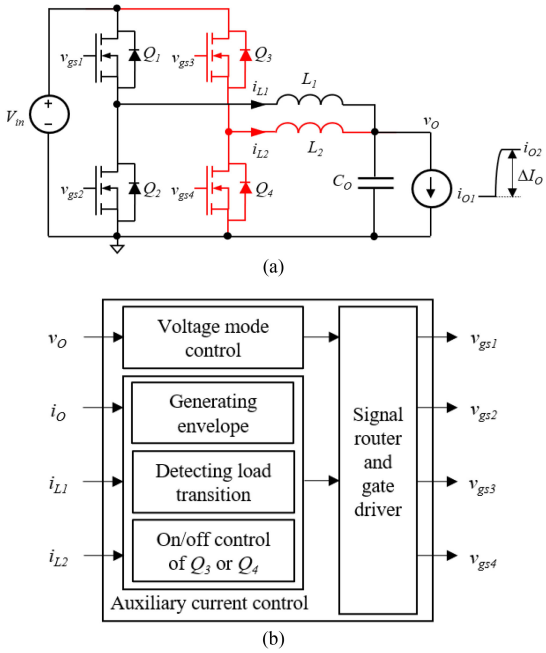

Fig. 1. (a) Main buck converter (Q_1, Q_2, and L_1) and auxiliary buck/boost converter (Q_3, Q_4, and L_2); the load current i_O varies with the limited slew rate. (b) Simplified control diagram of auxiliary current control.

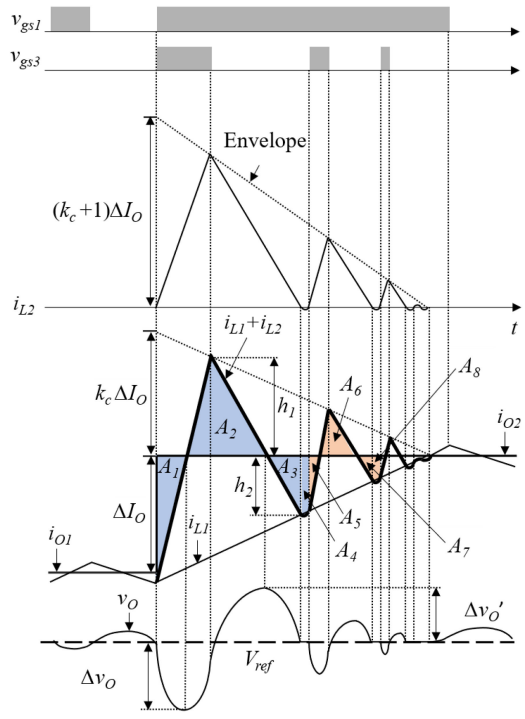

Fig. 2. Ideal currents and voltage waveforms of auxiliary current control when i_O is stepped up from i_{O1} to i_{O2}.

The ideal currents and voltages of the auxiliary current control are shown in Fig. 2. The literal ΔI_O is the magnitude of the i_O variation, or $i_{O2} - i_{O1}$, and V_{ref} is the target output voltage. The magnitude of i_{L2} is controlled by an envelope whose height is

$(k_c + 1)\Delta I_O$, where k_c is the envelope coefficient with an ideal implementation. The details of the operation and implementation of the control circuit are presented in [18].

In Fig. 2, area A_i represents the amount of charge that is charged to or discharged from C_O, and the v_O deviation is proportional to this area. The cycle-by-cycle CCB of C_O is satisfied by the envelope coefficient, k_c, and its condition is expressed as follows:

$$A_i + A_{i+2} = A_{i+1} \quad (i = 1,\ 5,\ 9,\ \cdots). \tag{1}$$

Notably, A_{i+3} is not considered in (1) because it is sufficiently smaller than A_i, A_{i+1}, and A_{i+2} in the practical implementation.

The coefficient k_c is derived from the geometry of i_{L1}, i_{L2} and ΔI_O shown in Fig. 2. The heights h_1 and h_2 are expressed by (2) and (3), assuming that v_O is constant as V_O, with negligible ripples during the transient

$$h_1 = \frac{k_c \Delta I_O L_1}{L_1 + (1 + k_c) L_2} \tag{2}$$

$$h_2 = \frac{\Delta I_O}{V_O} \frac{L_1 V_O - (V_{\text{in}} - V_O)(1 + k_c) L_2}{L_1 + (1 + k_c) L_2}. \tag{3}$$

Combining (2), (3), ΔI_O, and the slopes of i_{L1} and i_{L2}, reveals that k_c depends on V_{in}, V_O, L_1, and L_2, and not on ΔI_O, as expressed as

$$k_c = \frac{L_1 V_O - L_2 (V_{\text{in}} - 2V_O)}{L_1 V_O + L_2 (V_{\text{in}} - 2V_O)}. \tag{4}$$

By considering that the duty ratio of an ideal buck converter in the continuous conduction mode, D, is equal to V_O/V_{in}, (4) is rearranged as follows:

$$k_c = \frac{D(L_1 + 2L_2) - L_2}{D(L_1 + 2L_2) + L_2}. \tag{5}$$

Equation (5) implies that k_c is solely determined by D if L_1 and L_2 are set. Note that k_c is affected by the tolerance of the inductances. For example, k_c varies from -5.6% to 4.8% with $\pm 10\%$ tolerance of L_1 and L_2. However, this variation becomes even smaller and negligible if the other non-idealities explained in Section III are considered.

The undershoot Δv_O and overshoot $\Delta v_O{}'$ are proportional to A_1 and $A_2 - A_1$, respectively, as follows:

$$\Delta v_O = \frac{A_1}{C_O} = \frac{\Delta I_O^2 L_1 L_2}{2C_O (L_1 + L_2)(V_{\text{in}} - V_O)} \tag{6}$$

$$\Delta v_O{}' = \frac{A_2 - A_1}{C_O} = \frac{\Delta I_O^2 L_1 L_2 (L_1 V_O - L_2 V_{\text{in}})^2}{2C_O \{L_1 V_O - L_2 (V_{\text{in}} - V_O)\} (L_1 V_O + L_2 V_{\text{in}})^2}. \tag{7}$$

Ideally, voltages Δv_O and $\Delta v_O{}'$ should both be proportional to $\Delta I_O{}^2$.

Fig. 3(a) shows the plot of k_c versus D under the conditions given in Table I. The analyses and simulations described later in this paper employ the parameters given in Table I. The variation of k_c, or $\frac{dk_c}{dD}$, becomes considerable when D is relatively small.

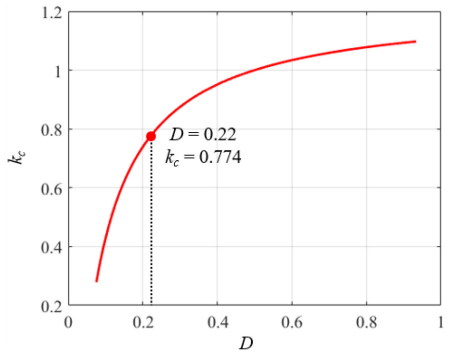

(a)

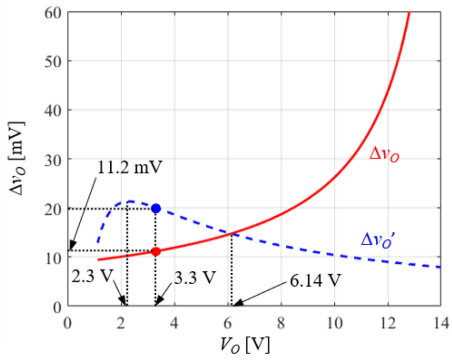

(b)

Fig. 3. Ideal relationships between variables under the conditions defined in Table I, (a) k_c versus D, (b) Δv_O (solid line) and $\Delta v_O{}'$ (dashed line) versus V_O.

TABLE I
CIRCUIT PARAMETERS USED IN SIMULATION AND EXPERIMENT

Parameter	Description
V_{in}	15 V
V_O	3.3 V
D	0.22
i_{O1}	4 A
i_{O2}	15 A
Switching frequency (f) of Q_1 and Q_2	200 kHz
L_1	10 µH
L_2	500 nH
C_O	220 µF

Fig. 3(b) shows Δv_O and $\Delta v_O{}'$ for various V_O values with the parameters given in Table I. The overshoot $\Delta v_O{}'$ is larger than the undershoot Δv_O if $V_O < 6.14$ V. For example, with V_O of 3.3 V, a Δv_O of 11.2 mV is expected, which is smaller than $\Delta v_O{}'$ of 20 mV. When $V_O < 2.3$ V, the overshoot $\Delta v_O{}'$ determined by $A_2 - A_1$, as in (7), increases because the increment of A_2 is larger than that of A_1. By contrast, when $V_O \geq 2.3$ V, the increment of A_1 is larger than that of A_2, and thus, $\Delta v_O{}'$ decreases. However, Δv_O dominates $\Delta v_O{}'$ if the time delay is considered as described in Section III-C.

Fig. 4 shows the simulated dynamics of the auxiliary current control when i_O is stepped up from 4 to 15 A ($\Delta I_O = 11$ A) with $k_c = 0.774$ using LTspice XVII. The number of switching cycles of the auxiliary converter was limited to 5 to avoid an excessive switching frequency and ensure a v_O deviation of less

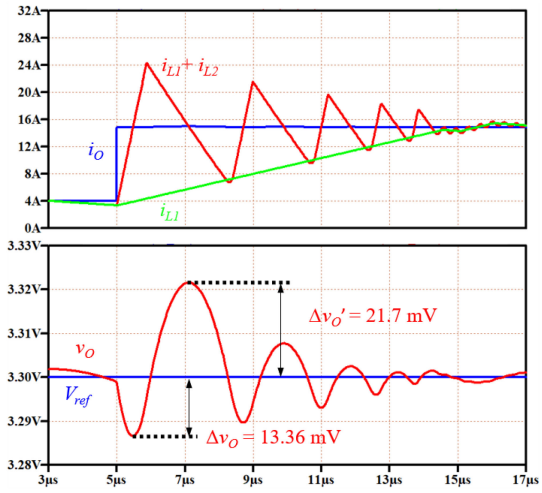

Fig. 4. Simulated response of auxiliary current control when $\Delta I_O = 11$ A and $k_c = 0.774$ in ideal implementation.

than 1.8 mV, which is the output voltage ripple in the steady state. The auxiliary current control exhibited Δv_O of 13.36 mV and Δv_O' of 21.7 mV. These values are different from those shown in Fig. 3(b) because the ripples of i_{L1} and v_O are not considered. Section III-B presents a detailed discussion on the effect of the ripple on the load transient response.

III. Analysis of Nonidealities of Auxiliary Current Control in Practical Implementation

The analysis presented in Section II highlights the error in the experimental results, which occurred because the nonidealities are not considered in the practical implementation. In this section, four representative nonideal factors, such as the ESR of C_O, ripples of i_{L1} and v_O, time delay in the control circuit at the beginning of the transient, and limited slew rate of i_O, are analyzed and their effect on the dynamics of v_O is quantified.

A. Equivalent Series Resistance of Output Capacitor

Fig. 5(a) shows the ESR of C_O, r_C. The literals v_C and i_C are the voltage and current of C_O, respectively. The output voltage v_O is derived as follows:

$$v_O = v_C + i_C(t)\, r_C = \frac{1}{C_O}\int i_C(t)\, dt + i_C(t)\, r_C. \quad (8)$$

The resistance r_C induces additional deviation of v_O, as shown in Fig. 5(b). The red solid curve represents the capacitor voltage v_C and the blue dashed curve denotes the output voltage v_O. The voltages Δv_C and Δv_C' are equal to the ideal undershoot Δv_O in (6) and the overshoot Δv_O' in (7), respectively. The deviations $\Delta v_{\rm ESR}$ and $\Delta v_{\rm ESR}$' are caused by r_C, as expressed as

$$\Delta v_{\rm ESR} = \Delta I_O r_C \quad (9)$$

and (10) shown at botttom of the next page.

The time intervals t_u and t_o, that is, when Δv_O and Δv_O' occur, are obtained by differentiating v_O with respect to time, as

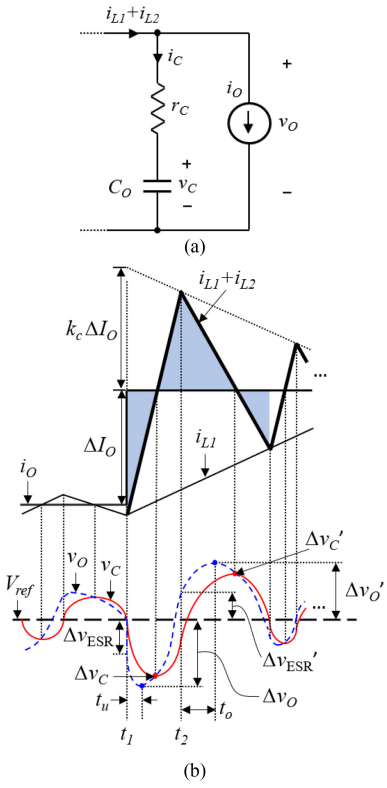

Fig. 5. (a) Output capacitor with r_C and (b) current and voltage waveforms including r_C when i_O is stepped up. The effect of r_C is exaggerated for clarity.

expressed as

$$t_u = \frac{\Delta I_O L_1 L_2 - C_O r_C (L_1 + L_2)(V_{\rm in} - V_O)}{(L_1 + L_2)(V_{\rm in} - V_O)} \quad (11)$$

and (12) as shown at bottom of the next page.

According to (8)–(12), Δv_O and Δv_O' in (6) and (7) are redefined as expressed in (13) and (14) shown at the bottom of next page, respectively.

Fig. 6 shows the plot of Δv_O in (13) and Δv_O' in (14) for various r_C. The undershoot Δv_O increases faster than Δv_O' as r_C increases. The overshoot Δv_O' is smaller than Δv_O when $r_C > 2.05$ mΩ.

In this article, C_O was implemented using twenty-two 10-μF multilayer ceramic capacitors in parallel, and r_C was negligibly small. Therefore, the effect of r_C is not considered in the discussion presented in the following sections.

B. Inductor Current and Output Voltage Ripples

The analysis presented in Section II assumes that the load transient occurs when i_{L1} is the minimum. However, the load current may transition at any instant in the switching period of the main buck converter. As mentioned in Section II, the deviation of v_O depends on i_{L1} and v_O at the instant of load transition. Specifically, the undershoot Δv_O is more prone to the instantaneous values of i_{L1} and v_O, as compared with the overshoot Δv_O'. Fig. 7 shows the waveforms of i_{L1} and v_O when $D < 0.5$. The literals Δi_{L1}, $\Delta v_{O\_\rm rp}$, and $\Delta v_{O\_\rm rp}$' denote the ripples of i_{L1}, v_O, and the instantaneous v_O when Q_1 turns

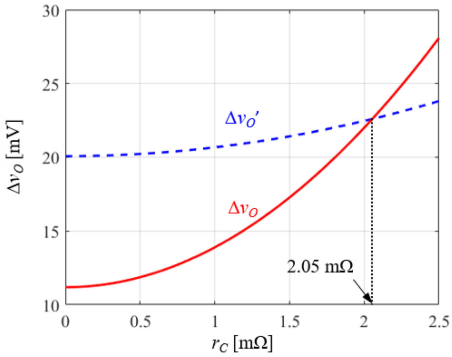

Fig. 6. Δv_O (solid line) and Δv_O' (dashed line) versus r_C.

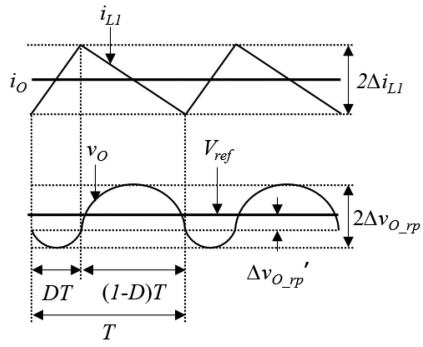

Fig. 7. Ripple current and voltage waveforms of buck converter when $D < 0.5$.

ON or OFF, respectively, and are expressed as

$$\Delta i_{L1} = \frac{V_O\,(1-D)}{2L_1 f} \tag{15}$$

$$\Delta v_{O\_\mathrm{rp}} = \frac{\Delta i_{L1}}{16C_O f} = \frac{V_O\,(1-D)}{16L_1C_O f^2} \tag{16}$$

$$\Delta v_{O\_\mathrm{rp}}{}' = \begin{cases} \left|\frac{V_O(1-D)(1-2D)}{16L_1C_O f^2}\right| & (0 < D < 0.5) \\ 0 & (D = 0.5) \\ \left|\frac{V_O D(1-D)}{16L_1C_O f^2}\right| & (0.5 < D < 1)\,. \end{cases} \tag{17}$$

In (17), the voltage ripple Δv_{O_rp}' depends on the range of D. This article focuses on the case of $D < 0.5$, which is the general case in POL applications.

The ripples Δi_{L1}, Δv_{O_rp}, and Δv_{O_rp}' are added to or subtracted from ΔI_O and Δv_O, and they affect the dynamic performance of the converter. To analyze the effect of Δi_{L1}, Δv_{O_rp}, and Δv_{O_rp}' on Δv_O, the four cases shown in Fig. 8 are considered. Fig. 8(a) shows the case wherein Q_1 is turned OFF and $i_{L1} = i_O$ at t_1. Fig. 8(b) shows the case wherein Q_1 is turned ON and $i_{L1} = i_O$ at t_1. Fig. 8(c) shows the case wherein Q_1 is turned ON and $i_{L1} = i_O + \Delta i_{L1}$ at t_1. Fig. 8(d) shows the case wherein Q_1 is turned OFF and $i_{L1} = i_O - \Delta i_{L1}$ at t_1. By manipulating (6) and (15)–(17), Δv_O in Fig. 8 can be derived as follows:

$$\mathrm{Fig.\,8(a)} : \Delta v_O = \frac{\Delta I_O^2 L_1 L_2}{2C_O\,(L_1+L_2)\,(V_{\mathrm{in}} - V_O)} - \Delta v_{O\_\mathrm{rp}} \tag{18}$$

$$\Delta v_{\mathrm{ESR}}{}' = \frac{\Delta I_O \left[\{L_1V_O - L_2\,(V_{\mathrm{in}} - V_O)\}\,\{\Delta I_O L_1 L_2 + 2C_O r_C\,(L_1+L_2)\,(V_{\mathrm{in}} - V_O)\,(L_1V_O + L_2V_O)\} - \Delta I_O L_1 L_2 (L_1V_O + L_2V_O)^2\right]}{2C_O\,(L_1+L_2)\,(V_{\mathrm{in}} - V_O)\,(L_1V_O + L_2V_O)^2} \tag{10}$$

$$t_o = \frac{\Delta I_O L_1 L_2\,\{L_1V_O - L_2\,(V_{\mathrm{in}} - V_O)\} - C_O r_C\,(L_1V_O + L_2V_{\mathrm{in}})\,\{L_1V_O - L_2\,(V_{\mathrm{in}} - V_O)\}}{(L_1V_O + L_2V_{\mathrm{in}})\,\{L_1V_O - L_2\,(V_{\mathrm{in}} - V_O)\}} \tag{12}$$

$$\Delta v_O = \frac{1}{C_O}\int_{t_1}^{t_u}\left[\Delta I_O - \left\{\frac{(L_1+L_2)\,(V_{\mathrm{in}} - V_O)}{L_1L_2}\right\} t\right] dt + r_C\left[\Delta I_O - \left\{\frac{(L_1+L_2)\,(V_{\mathrm{in}} - V_O)}{L_1L_2}\right\} t_u\right]$$

$$= \begin{cases} \frac{\Delta I_O^2 L_1^2 L_2^2 + C_O^2 r_C^2 (L_1+L_2)^2 (V_{\mathrm{in}} - V_O)^2}{2C_O L_1 L_2 (L_1+L_2)(V_{\mathrm{in}} - V_O)} & (t_u > 0) \\ \Delta v_{\mathrm{ESR}} & (t_u = 0) \end{cases} \tag{13}$$

$$\Delta v_O{}' = \frac{1}{C_O}\left[\begin{array}{l} \int_{t_u}^{t_2}\left\{\frac{(L_1+L_2)(V_{\mathrm{in}} - V_O)}{L_1L_2}\right\} t\,dt \\ + \int_{t_2}^{t_o}\left[\left\{\frac{L_2(V_{\mathrm{in}} - V_O) - L_1V_O}{L_1L_2}\right\} t + h_1\right] dt \\ - \int_{t_1}^{t_u}\left[\Delta I_O - \left\{\frac{(L_1+L_2)(V_{\mathrm{in}} - V_O)}{L_1L_2}\right\} t\right] \end{array}\right] + r_C\left[\begin{array}{l} \left\{\frac{(L_1+L_2)(V_{\mathrm{in}} - V_O)}{L_1L_2}\right\} t_u \\ + \left\{\frac{L_2(V_{\mathrm{in}} - V_O) - L_1V_O}{L_1L_2}\right\} t_o + 2h_1 - \Delta I_O \end{array}\right]$$

$$= \begin{cases} \frac{\Delta I_O^2 L_1^2 L_2^2 (L_1V_O - L_2V_{in})^2 + C_O^2 r_C^2 (L_1V_O + L_2V_{\mathrm{in}})^2 \{L_1V_O - L_2(V_{\mathrm{in}} - V_O)\}^2}{2C_O L_1 L_2 \{L_1V_O - L_2(V_{\mathrm{in}} - V_O)\}(L_1V_O + L_2V_{\mathrm{in}})^2} & (t_o > 0) \\ \Delta v_{\mathrm{ESR}}{}' & (t_o = 0) \end{cases} \tag{14}$$

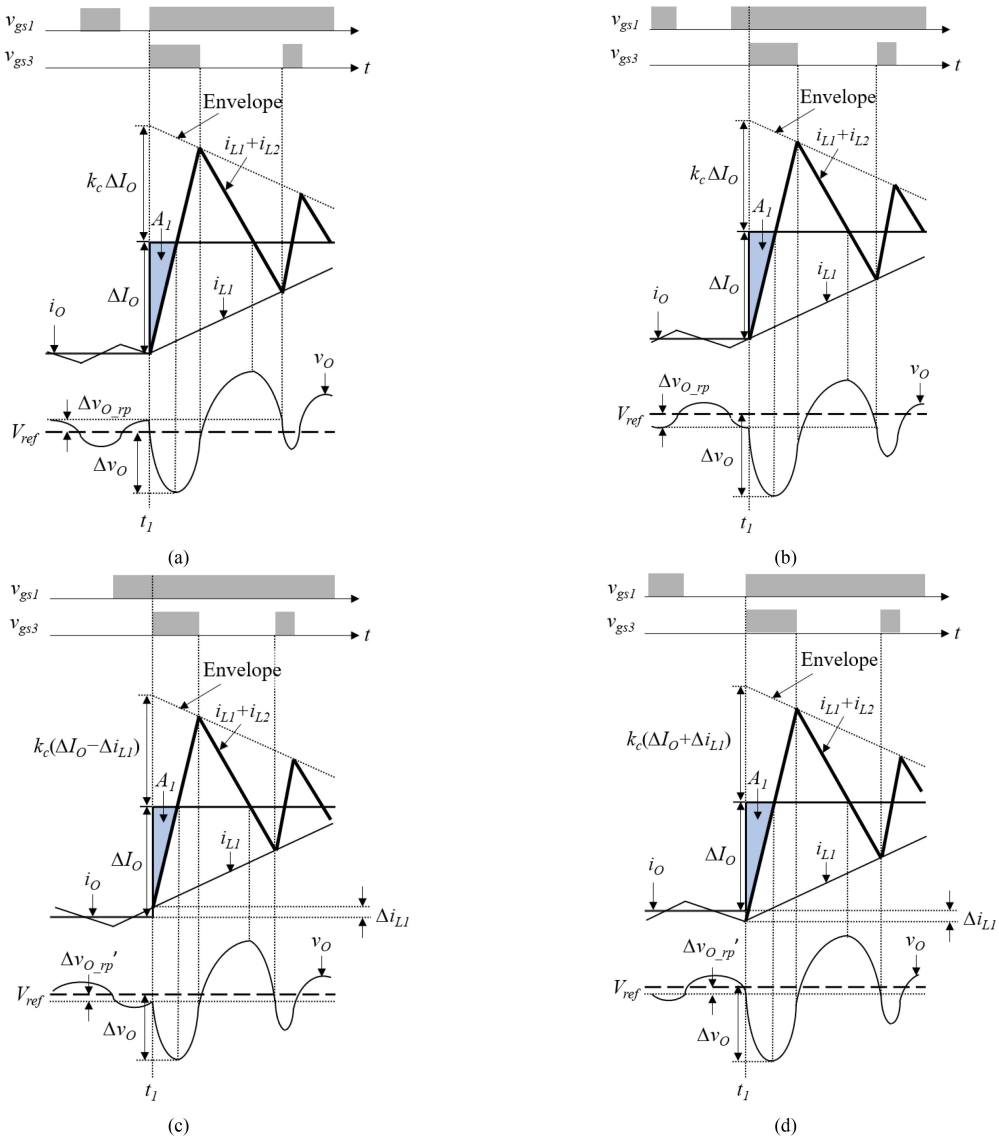

Fig. 8. Effect of ripple on Δv_O when i_O is stepped up. (a) Q_1 is OFF and $i_{L1} = i_O$ at t_1. (b) Q_1 is ON and $i_{L1} = i_O$ at t_1. (c) Q_1 is ON and $i_{L1} = i_O + \Delta i_{L1}$ at t_1. (d) Q_1 is OFF and $i_{L1} = i_O - \Delta i_{L1}$ at t_1.

$$\text{Fig. 8(b)} : \Delta v_O = \frac{\Delta I_O^2 L_1 L_2}{2C_O\left(L_1+L_2\right)\left(V_{\text{in}}-V_O\right)} + \Delta v_{O\_\text{rp}} \tag{19}$$

$$\text{Fig. 8(c)} : \Delta v_O = \frac{\left(\Delta I_O - \Delta i_{L1}\right)^2 L_1 L_2}{2C_O\left(L_1+L_2\right)\left(V_{\text{in}}-V_O\right)} + \Delta v_{O\_\text{rp}}{}' \tag{20}$$

$$\text{Fig. 8(d)} : \Delta v_O = \frac{\left(\Delta I_O + \Delta i_{L1}\right)^2 L_1 L_2}{2C_O\left(L_1+L_2\right)\left(V_{\text{in}}-V_O\right)} + \Delta v_{O\_\text{rp}}{}'. \tag{21}$$

Fig. 9(a) shows Δv_O in (6) and (18)–(21) versus ΔI_O. When $\Delta I_O < 4.4$ A, Δv_O in (18) (green curve) becomes negative because ΔvO_rp is larger than the undershoot by A_1. If $\Delta I_O >$ 9 A, Δv_O in (20) (magenta curve) is smaller than Δv_O in the ideal case expressed in (6) (black dashed curve). When $\Delta I_O = 11$ A, as shown in Fig. 9(a), the Δv_O values in (18)–(21) are 9.36, 13.02, 10.95, and 13.56 mV, respectively. For a conservative design, the Δv_O values in (19) and (21) should be considered because they are always larger than the ideal Δv_O in (6). The simulation in Fig. 4 was implemented using the case shown in Fig. 8(d), because Δv_O in (21) is the largest among the four cases when ΔI_O is 11 A. The waveshapes in Figs. 4 and 8(d) are analogous, and the calculated value of Δv_O for 13.56 mV in Fig. 9(a) is similar to the simulated value of 13.36 mV in Fig. 4.

Fig. 9(b) quantifies the effect of ripples of i_{L1} and v_O on Δv_O for the cases shown in Fig. 8(b) and (d). The solid line represents the case shown in Fig. 8(b), calculated by (6) and (19). The dashed line is for the case shown in Fig. 8(d) by (6) and (21). When $\Delta I_O > 6.44$ A, the dashed line is larger than the solid line because Δi_{L1} and Δv_{O_rp}' affect Δv_O more than Δv_{O_rp}. When $\Delta I_O = 11$ A, the effects of the ripples in Fig. 8(b) and (d) are 14.04% and 17.48%, respectively. These values may

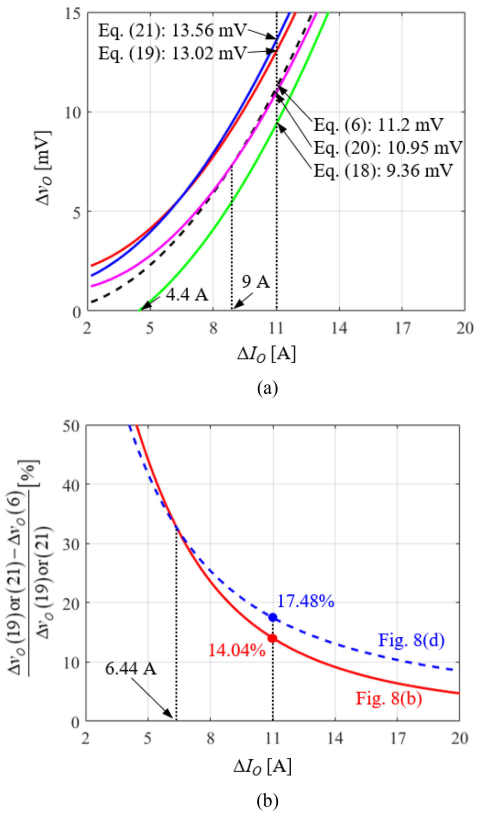

Fig. 9. (a) Δv_O and (b) effect of ripples on v_O versus ΔI_O.

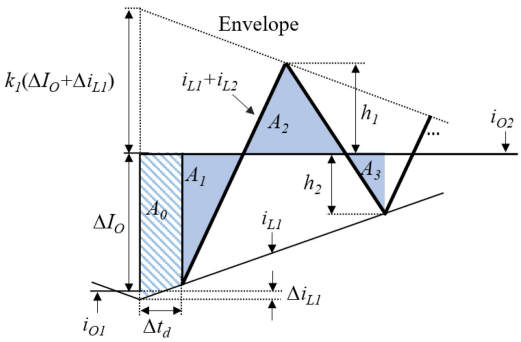

Fig. 10. Current waveforms for deriving k_1, Δv_O, and Δv_O' with $\Delta t_d > 0$.

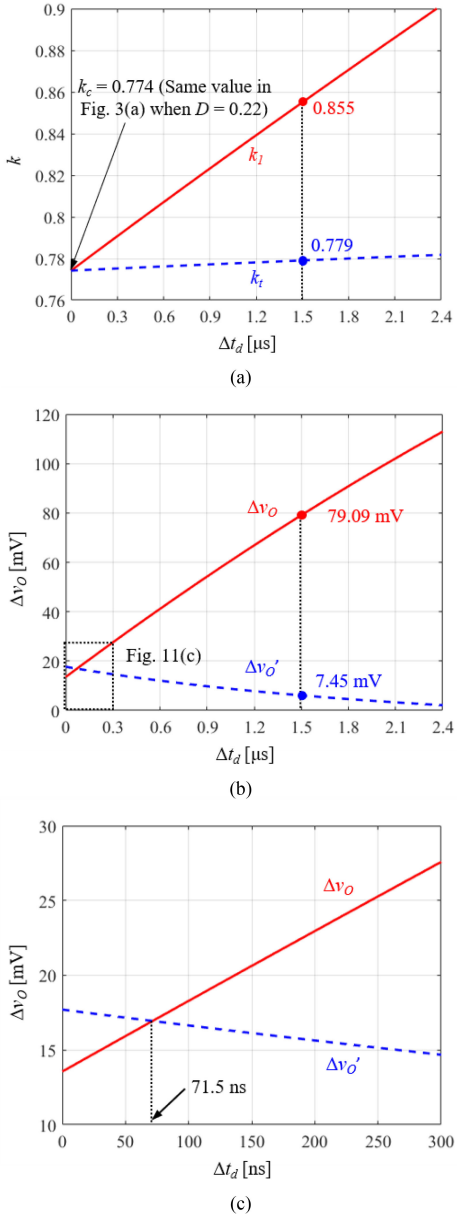

Fig. 11. (a) k_1 (solid line) and k_t (dashed line). (b) Δv_O (solid line) and Δv_O' (dashed line) versus Δt_d by k_1. (c) Enlarged plot of Fig. 11(b).

not appear to be negligible with regard to the precision of the analysis. However, the time delay in the control circuit reduces the significance of the ripple, as given in Section III-C.

C. Time Delay

In practice, there exists a time delay Δt_d between the load transient and the first turn-on of Q_3, owing to the signal propagation delays in the control circuit, as shown in Fig. 10. The hashed trapezoid A_0 caused by Δt_d in Fig. 10 is expressed as follows:

$$A_0 = \left\{ \Delta I_O + \Delta i_{L1} - \frac{\Delta t_d \left(V_{\text{in}} - V_O\right)}{2L_1} \right\} \Delta t_d. \tag{22}$$

The condition for the CCB in the first switching cycle is expressed as follows:

$$A_0 + A_1 + A_3 = A_2. \tag{23}$$

The heights h_1 and h_2 in (2) and (3) are redefined as expressed in (24) and (25) with the ripple current Δi_{L1} and positive Δt_d, respectively

$$h_1 = \frac{k_1 \left\{ L_1 \left(\Delta I_O + \Delta i_{L1} \right) - \Delta t_d \left(V_{\text{in}} - V_O \right) \right\}}{L_1 + \left(1 + k_1\right) L_2}. \tag{24}$$

By combining (22), (24), and (25), ΔI_O, and the slopes of i_{L1} and i_{L2}, the k_1 satisfying (23) can be derived as

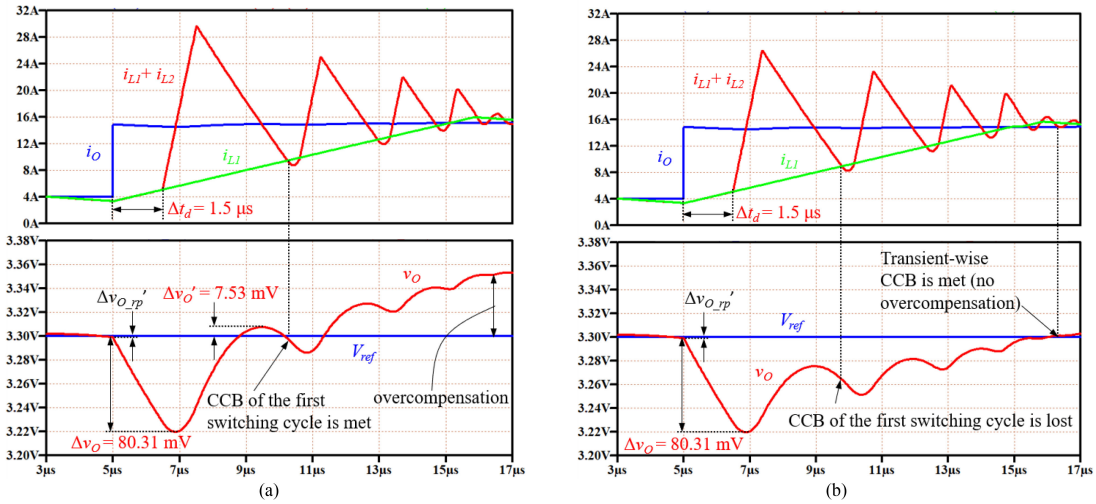

Fig. 12. Simulated response of auxiliary current control when $\Delta I_O = 11$ A and $\Delta t_d = 1.5$ μs. (a) CCB during the first switching cycle is achieved by $k_1 = 0.855$. (b) CCB is achieved at the end of the transient by $k_t = 0.779$.

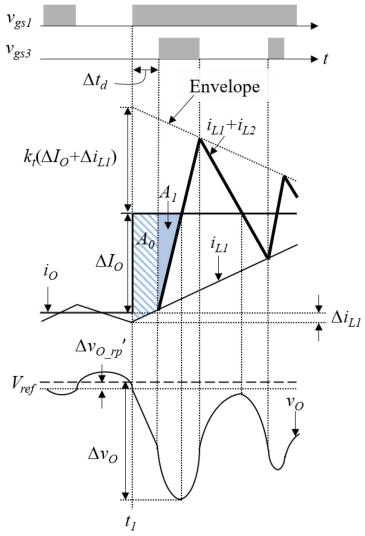

Fig. 13. Effect of ripple on Δv_O when i_O is stepped up, Q_1 is OFF, $i_{L1} = i_O - \Delta i_{L1}$ at t_1, and $\Delta t_d > 0$.

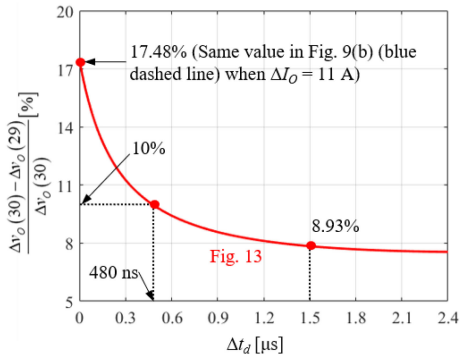

Fig. 14. Effect of the ripples and time delay on Δv_O versus Δt_d.

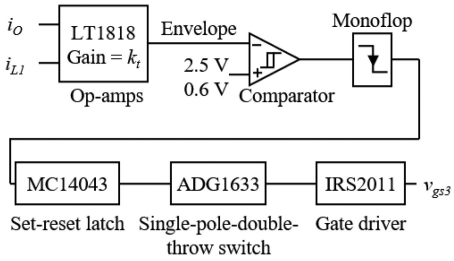

Fig. 15. Generating the first turn-on signal of Q_3 when i_O is stepped up.

in (26). Equation (25) is shown at bottom of the next page.

$$k_1 = \frac{\beta L_2^2 (V_{\text{in}} - V_O) - \alpha V_O (L_1 + L_2)}{L_2 [\alpha V_O - \beta \{L_1 V_O + L_2 (V_{\text{in}} - V_O)\}]} \tag{26}$$

The subscript "1" of k_1 implies that the coefficient satisfies the CCB in the first switching cycle. In (26), α is the same as in (27) and β is same as

$$\beta = L_1 V_{\text{in}} \{L_1 (\Delta I_O + \Delta i_{L1}) - \Delta t_d (V_{\text{in}} - V_O)\} \tag{28}$$

$$\Delta v_O = \frac{L_1 L_2 \Delta I_O^2 + 2 L_1 \Delta I_O \Delta t_d (V_{\text{in}} - V_O) - \Delta t_d^2 (V_{\text{in}} - V_O)^2}{2 C_O (L_1 + L_2)(V_{\text{in}} - V_O)} \tag{29}$$

Equation (27) is shown at bottom of the next page.

Fig. 11(a) shows the plot of k_1 versus Δt_d. Non-idealities such as ripples and Δt_d results in $k_1 > k_c$. When $\Delta t_d > 0$, k_1 increases almost linearly, even though (26)–(28) appear complicated.

The voltage deviations Δv_O and Δv_O' in (6) and (7) are also redefined in (29)–(31), with consideration to Δt_d and the ripples discussed in Section III-B. Notably, Δv_O is defined in two ways in (29) and (30). Δv_O in (29) includes the effect of Δt_d only and becomes identical to (6) when $\Delta t_d = 0$; Δv_O in (30) and Δv_O' in (31) include the effect of both Δt_d and the ripples discussed in Section III-B. These definitions are used later in this paper to quantify the effect of each nonideality on Δv_O.

Fig. 11(b) shows the plot of Δv_O and Δv_O' versus Δt_d. By comparing (30) and (31) as shown at bottom of this page, it can be found that Δt_d determines whether $\Delta v_O > \Delta v_O$'. According to the enlarged plot shown in Fig. 11(c), Δv_O is larger than Δv_O' if $\Delta t_d > 71.5$ ns as mentioned in Section II.

The coefficient k_1 satisfies the CCB in the first switching cycle but overcompensates v_O at the end of the transient operation, which should be avoided because it may deteriorate the fluctuation of v_O after the operation of the auxiliary circuit. This overcompensation is eliminated by decreasing k_1, that is, by substituting k_1 into k_t. The new envelope coefficient k_t (dashed line) in Fig. 11(a) loses the cycle-by-cycle CCB but obtains the transient-wise CCB. As shown in Fig. 11(a), the time Δt_d has a weaker effect on k_t than on k_1.

Fig. 12 compares the simulated dynamics of the auxiliary current control when $\Delta t_d = 1.5$ μs. The coefficients k_1 and k_t were set to 0.855 and 0.779, respectively, as shown in Fig. 11(a). When $\Delta I_O = 11$ A, the auxiliary current control by k_1 and k_t both exhibited the same Δv_O because the envelope coefficients do not affect Δv_O, as in (30). In Fig. 12(a), the CCB for the first switching cycle was satisfied but v_O was overcompensated. By contrast, in Fig. 12(b), v_O converged to $V_{\rm ref}$ at the end of the transient operation. The simulated Δv_O of 80.31 mV and Δv_O' of 7.53 mV, shown in Fig. 12(a), are similar to the calculated Δv_O of 79.09 mV and Δv_O' of 7.45 mV, shown in Fig. 11(b), respectively.

Fig. 13 shows the case where Δt_d maximally affects the v_O deviation in conjunction with Δi_L and $\Delta v_{O\_\rm rp}$' analyzed in Section III-B. In other words, the load transition occurs when i_{L1} is minimum, which is similar to the case shown in Fig. 8(d), but includes the maximum A_0 caused by Δt_d. Fig. 14 quantifies the contribution of the ripple for various Δt_d values by subtracting (29) from (30). The effect of the ripple on Δv_O is less than 10% when $\Delta t_d \geq 480$ ns. When $\Delta t_d = 1.5$ μs, which is the case of the experiment described in Section IV, ripples ratio to Δv_O is 8.93% in the case shown in Fig. 13. Additionally, when $\Delta t_d = 0$, the value of 17.48% agrees with that shown in Fig. 9(b).

Fig. 15 shows a simplified control circuit to explain the range of Δt_d. Full circuit diagram is available in [18]. The load transition, i.e., the abrupt increase of i_O, is firstly detected by sensing i_{L1} and i_O. A set of operational amplifiers then generates the envelope described in Figs. 2, 8, 10, and 13. The first turn-ON signal of Q_3 is generated by a hysteresis comparator, monoflop, set-reset latch, single-pole-double-throw switch, and gate driver. Propagation delays of the cost-effective off-the-shelf ICs utilized in Fig. 15 are given in Table II, which sums up to 600 ns approximately. Finite slope of the rising edge of the envelope waveshape and intrinsic delay of the monoflop provide another 600-ns delay variation, and Δt_d becomes 1.2 μs. The maximum Δt_d in this article is set as 2.4 μs which is twice 1.2 μs.

TABLE II
PROPAGATION DELAYS OF THE ICS IN Fig. 15

Component	Part name (manufacturer)	Propagation delay in nanoseconds
Gate driver	IRS2011 (Infineon)	80 (typical)
Op-amps for generating envelope	LT1818 (Analog Devices)	2 (typical)
Comparator	LT1720 (Analog Devices)	1 (maximum)
Logic inverter in monoflop	SN74LVC2G14DBVR (Texas Instruments)	4.7 (maximum)
NAND gates in monoflop	74LVC2G00DP (Nexperia)	4.2 (maximum)
Set-reset latch	MC14043BDG (ON Semiconductor)	350 (maximum)
Single-pole-double-throw switch	ADG1633BRUZ (Analog Devices)	151 (maximum)

D. Slew Rate of Load Current

The load current i_O cannot be a perfect step owing to the parasitic components in the practical implementation. The switched resistor shown in Fig. 16(a) was built and used in this article to achieve an i_O with a sufficiently high slew rate. Its equivalent circuit is shown in Fig. 16(b); C_O and R_{L1} are replaced by a dc voltage source V_O, and the parasitic components of R_{L2} and Q_L that limit the slew rate of i_O are modeled as $L_{\rm eq}$. The switch Q_L is substituted by the ideal switch $Q_{\rm ideal}$. This modeling approach approximates the transient i_O as an exponential curve.

$$h_2 = \frac{\{L_1(\Delta I_O + \Delta i_{L1}) - \Delta t_d(V_{\rm in} - V_O)\}\{L_1 V_O - L_2(1+k_1)(V_{\rm in} - V_O)\}}{V_O L_1\{L_1 + (1+k_1)L_2\}} \tag{25}$$

$$\alpha = \sqrt{L_1^3 L_2 V_{\rm in}\left[L_1 L_2 V_{\rm in}(\Delta I_O + \Delta i_{L1})^2 + \Delta t_d V_O(V_{\rm in} - V_O)\{2L_1(\Delta I_O + \Delta i_{L1}) - \Delta t_d(V_{\rm in} - V_O)\}\right]} \tag{27}$$

$$\Delta v_O = \frac{L_1 L_2(\Delta I_O + \Delta i_{L1})^2 + 2\Delta t_d\{(L_1\Delta I_O - L_2\Delta i_{L1})(V_{\rm in} - V_O)\} - \Delta t_d^2(V_{\rm in} - V_O)^2}{2C_O(L_1 + L_2)(V_{\rm in} - V_O)} + \Delta v_{O\_\rm rp}' \tag{30}$$

$$\Delta v_O' = \frac{L_1^2 L_2 h_1^2 V_{\rm in}}{2C_O(L_1 + L_2)(V_{\rm in} - V_O)\{L_2(V_{\rm in} - V_O) - L_1 V_O\}} + \frac{L_2\{\Delta t_d(V_O - V_{\rm in}) + L_1(\Delta I_O + \Delta i_{L1})\}^2}{2L_1 C_O(L_1 + L_2)(V_{\rm in} - V_O)} + \frac{\Delta t_d\{2L_1\Delta I_O - L_2\Delta i_{L1} + \Delta t_d(V_O - V_{\rm in}) + L_1^2\Delta i_{L1}^2\}}{2L_1 C_O} - \Delta v_{O\_\rm rp}' \tag{31}$$

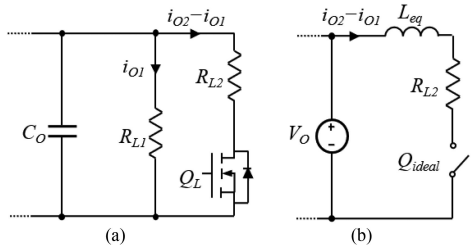

Fig. 16. Switched resistor to realize sufficiently high slew rate of i_O. (a) Implementation. (b) Equivalent circuit.

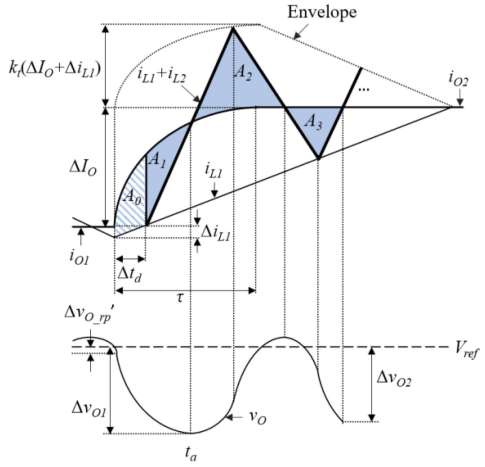

Fig. 17. Current and voltage waveforms with $\Delta t_d > 0$ and limited slew rate.

The exponentially increasing i_O affects the envelope as shown in Fig. 17. The time constant τ was selected as $5L_{\text{eq}}/R_{L2}$, during which i_O reached 99% of i_{O2}. The undershoots Δv_{O1} and Δv_{O2} are the maximum voltage deviations in the first and second switching cycles, respectively. The time t_a is when $i_{L1}+i_{L2}$ and i_{O2} intersect or (32) is satisfied

$$i_{O2}(t_a) = i_{L1}(t_a) + i_{L2}(t_a - \Delta t_d) - \Delta i_{L1}. \tag{32}$$

The coefficient k_t for accomplishing the transient-wise CCB is determined as follows:

$$A_0 + \sum_{i=1}^{N} A_{2i-1} = \sum_{i=1}^{N} A_{2i} \tag{33}$$

where N is the number of switching cycles of the auxiliary converter during the transient.

The first undershoot Δv_{O1} is determined by areas A_0 and A_1, as expressed in (34). The mathematical expressions of k_t and Δv_{O2} with regard to Δt_d and the limited slew rate of i_O are lengthy and counterintuitive. Instead, Fig. 18(a) shows the plot of k_t for various τ values when Δt_d is 1.2, 1.5, 1.8, and 2.1 μs. This plot was obtained by numerically analyzing (32) and (33). The coefficient k_t, which satisfies the transient-wise CCB, decreases to or increases from the black dashed line, which indicates the set of local minima or $\frac{dk_t}{d\tau} = 0$. For example, k_t with Δt_d of 1.5 μs (the blue line indicates the experimental case shown in

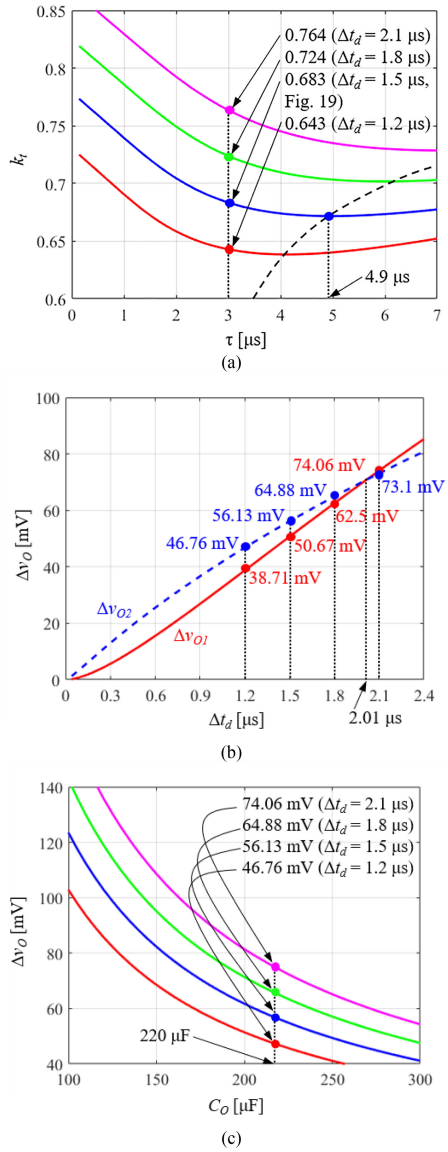

Fig. 18. (a) k_t versus τ. (b) Δv_{O1} (red solid line) and Δv_{O2} (blue dashed line) versus Δt_d when $\tau = 3$ μs. (c) Δv_O versus C_O when $\tau = 3$ μs.

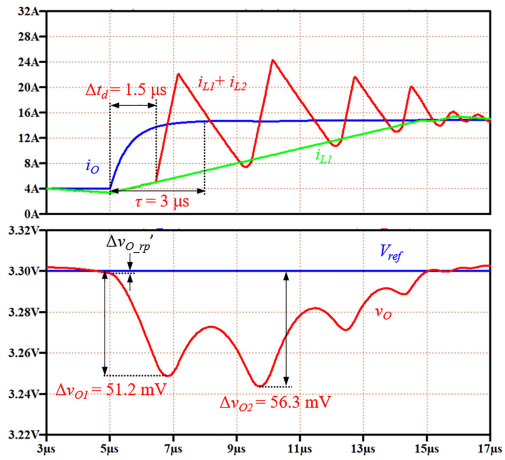

Fig. 19. Simulated dynamics of auxiliary current control by $k_t = 0.683$ when $\Delta I_O = 11$ A, $\Delta t_d = 1.5$ μs, and $\tau = 3$ μs.

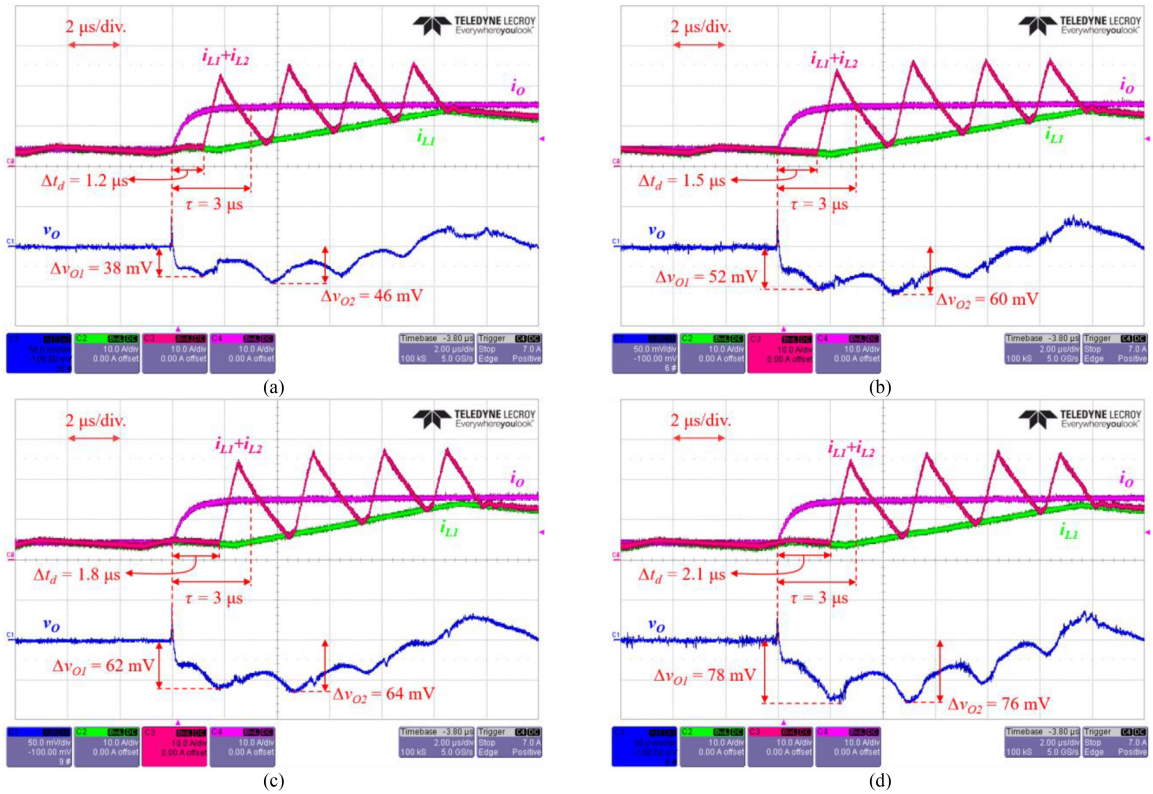

Fig. 20. Experimental waveforms of the auxiliary current control technique when i_O was stepped up from 4 A to 15 A ($\Delta I_O = 11$ A) and $\tau = 3$ μs; trace i_O (magenta), trace $i_{L1}+i_{L2}$ (red), and i_{L1} (green) are in 10 A/div; trace v_O (blue) is in 50 mV/div with ac coupling. The time scale is 2 μs/div. (a) $\Delta t_d = 1.2$ μs. (b) $\Delta t_d = 1.5$ μs. (c) $\Delta t_d = 1.8$ μs. (d) $\Delta t_d = 2.1$ μs.

Section IV) decreases when $\tau < 4.9$ μs and increases when $\tau \geq 4.9$ μs.

Fig. 18(b) shows Δv_{O1} and Δv_{O2} versus Δt_d. The undershoot Δv_{O2} with a τ value of 3 μs is larger than Δv_{O1} if $\Delta t_d < 2.01$ μs. Hence, the maximum undershoot Δv_O is expressed as follows:

$$\begin{aligned}\Delta v_{O1} &= \frac{A_0 + A_1}{C_O} + \Delta v_{O\_\mathrm{rp}}{}' \\ &= \frac{1}{C_O}\left[\int_0^{\Delta t_d}\left\{i_{O2}\left(1-e^{-\frac{5}{\tau}t}\right) - i_{L1}(t) - \Delta i_{L1}\right\}dt \right. \\ &\quad \left. + \int_{\Delta t_d}^{t_a}\left[\begin{array}{l}\left\{i_{O2}\left(1-e^{-\frac{5}{\tau}t}\right) - i_{L1}(t) - \Delta i_{L1}\right\} \\ +\left\{\left(i_{L2} - \Delta i_{L1}\right)(t-\Delta t_d)\right\}\end{array}\right]dt\right] \\ &\quad + \Delta v_{O\_\mathrm{rp}}{}' \qquad (34)\end{aligned}$$

$$\Delta v_O = \begin{cases}\Delta v_{O1}\,(\Delta t_d \geq 2.01\,\mu\mathrm{s}) \\ \Delta v_{O2}\,(\Delta t_d < 2.01\,\mu\mathrm{s}).\end{cases} \qquad (35)$$

Fig. 18(c) shows the plots of Δv_O versus C_O for Δt_d values of 1.2, 1.5, 1.8, and 2.1 μs when $\tau = 3$ μs. If $C_O = 220$ μF, Δv_O is 46.76, 56.13, 64.88, and 74.06 mV when Δt_d is 1.2, 1.5, 1.8, and 2.1 μs, respectively. The capacitance of C_O is reduced if Δt_d becomes smaller while maintaining the same Δv_O.

Fig. 19 shows the simulated response of the auxiliary current control when $\Delta I_O = 11$ A, $\Delta t_d = 1.5$ μs, $\tau = 3$ μs, and $k_t = 0.683$. The simulated Δv_{O1} of 51.2 mV and Δv_{O2} of 56.34 mV were similar to the estimated values of 50.67 and 56.13 mV in Fig. 18(b) with Δt_d of 1.5 μs, respectively.

TABLE III
COMPARISON OF UNDERSHOOTS IN ANALYSIS AND EXPERIMENT

Δt_d (μs)	k_t	Δv_{O1} (mV)		Δv_{O2} (mV)	
		Analysis	Experiment	Analysis	Experiment
1.2	0.643	38.71	38	46.76	46
1.5	0.683	50.67 51.2 (sim.)	52	56.13 56.3 (sim.)	60
1.8	0.724	62.5	62	64.88	64
2.1	0.764	74.06	78	73.1	76

IV. EXPERIMENTAL VERIFICATION

Prototype hardware was built to realize auxiliary current control with the parameters given in Table I. Selection of Q_3, Q_4, and L_2 are explained in the Appendix. The details regarding the implementation of the prototype are provided in [18].

Fig. 20 shows the experimental results of i_O (magenta trace), $i_{L1}+i_{L2}$ (red), i_{L1} (green), and v_O (blue) of the auxiliary current control for various Δt_d. The time constant τ was 3 μs, as in the simulation described in Section III-D. The measured undershoots Δv_{O1} and Δv_{O2} in Fig. 20(b) are analogous to the simulated ones in Fig. 19.

Table III compares the undershoots obtained via analyses [values shown in Fig. 18(b)] and the experiment (measured values

TABLE IV
PERFORMANCE COMPARISON WITH THE CONVENTIONAL CONTROL SCHEMES IN PRACTICAL IMPLEMENTATION

	Ref. [7]	Ref. [8]	Ref. [9]	Ref. [10]	Ref. [11]	Ref. [16]	Ref. [21]	This work
Control scheme	TOC	Sequence switching control	Load-side gyrator circuit	Bidirectional buck/boost converter	Resistive circuit	Resonant circuit	Coupled inductor switching	Bidirectional buck/boost converter
Non-idealities considered in analysis	ESR, ripple, Δt_d	Δt_d	Ripple	Ripple	Δt_d	None	ESR, slew rate	ESR, ripple, Δt_d, slew rate
Auxiliary components	None	Switch: 4 Inductor: 1 Resistor: 1	Switch: 12 Inductor: 3 Capacitor: 6	Switch: 2 Inductor: 1 Capacitor: 1	Switch: 4 Resistor: 4	Switch: 4 Inductor: 4 Capacitor: 2	Switch: 2 Inductor: 1 Capacitor: 1	Switch: 2 Inductor: 1
Input voltage [V]	5	24	12	12	10	12	12	15
Output voltage [V]	2.5	12	1.5	5	5	5	3.3	3.3
Switching frequency [kHz]	400	100	500	200	66	200	100	200
Main inductor [μH]	1	100	1.3	10	100	10	6.3	10
Auxiliary inductor [nH]	None	14500	10	420	None	60	100	500
Main capacitor [μF]	235	30	150	47	265	280	330	220
ESR [mΩ]	1	Not found	Not found	Not found	Not found	< 1	130	< 0.1
Auxiliary capacitor [μF]	None	None	20, 0.3	40	None	0.8, 1	100	None
Estimated max. output voltage ripple [mV]	2.08	12.5	1.68	9.7	1.35	1.63	7.19	1.83
Time delay [μs]	1.875	1	Not found	Not found	Not found	Not found	Not found	1.2–2.1
Load [A]	0–5	1.5–4.5	1.5–11.5 4.5–11.5	1–10	0.4–3.6	5–10	1–30	4–15
Measured voltage deviation [mV]	105	360	60 40	80	Not found	100	135	46–78

in Fig. 20). The envelope coefficients k_t for various Δt_d values are equal to those shown in Fig. 18(a). The good agreement between the compared values demonstrates the precision of the analysis presented in Section III. For the case of $\Delta t_d = 1.5$ μs, the simulated undershoots in Fig. 19 exhibited an even smaller error relative to the analysis. Notably, Δv_{O1} was smaller than Δv_{O2} when $\Delta t_d < 2.01$ μs, as shown in Fig. 20(a)–(c) and assumed in Fig. 18(b). However, in Fig. 20(d) wherein Δt_d is 2.1 μs, Δv_{O1} became larger than Δv_{O2}, as shown in Fig. 18(b). These observations are in good agreement with the explanation provided in Section III-D.

The proposed control method is compared with the conventional ones in Table IV. The work in this article includes the most nonideal characteristics such as ESR, inductor current and output voltage ripples, Δt_d, and the slew rate of the load current. The part count of the auxiliary components of the proposed method is the smallest.

V. CONCLUSION

This article presented an in-depth analysis on the dynamic response of a buck converter with auxiliary current control. The effect of non-idealities, such as the ESR of the output capacitor, main inductor current and output voltage ripples, time delay of the control circuitry, and the limited slew rate of the load current, was analyzed to achieve the transient-wise CCB. The following conclusions were drawn from this article.

1) The effect of the ripples of the main inductor current and output voltage is less than that of the time delay in the control circuit.
2) This time delay may cause the overshoot of the output voltage to exceed the undershoot, although the load current increases abruptly.
3) The limited slew rate of the load current combined with the time delay may force the maximum undershoot to occur at the second switching cycle of the auxiliary converter. The envelope coefficient k_t was derived to achieve the transient-wise CCB with three nonidealities such as the ripples, time delay, and the limited slew rate.

Finally, there was good agreement between the analyzed output voltage deviation obtained via the simulation and the experiment.

The future work includes the implementation that minimizes the effect of nonideal characteristics and suppresses Δv_O. Increasing the switching frequency of the main converter is one

of the options since it reduces the output voltage and inductor current ripples. Reducing Δt_d is also an effective design to mitigate the output voltage fluctuation. Utilization of digital controller IC can be a good candidate for smaller Δt_d.

APPENDIX

Current stress should be considered in selecting Q_3 and Q_4. As ΔI_O and the rate of occurrence of the load transient increase, the current rating of Q_3 and Q_4 should also be increased. In the prototype hardware, Q_3 and Q_4 were realized by the same field-effect transistor (FETs) used as Q_1 and Q_2, STP140N6F7. This is a conservative design implying that the auxiliary converter may experience the same stress with the main converter.

The auxiliary inductance L_2 is determined by trading off Δv_O and the power loss of Q_3 and Q_4. Smaller L_2 is preferred to suppress Δv_O, while it increases switching and gate driving loss of Q_3 and Q_4. Excessively small L_2 may even cause inaccurate operation of Q_3 and Q_4 due to the Δt_d of ICs. The range of L_2 is expressed as

$$\frac{V_O\left(V_{\text{in}}-V_O\right)}{V_{\text{in}} f_{\max}\left(\Delta I_O+h_1\right)} \leq L_2 \leq \frac{V_O\left(V_{\text{in}}-V_O\right)}{V_{\text{in}} f_{\min}\left(\Delta I_O+h_1\right)} \tag{36}$$

where $f_{\max}$ and $f_{\min}$ are the maximum and minimum switching frequency of Q_3 and Q_4, respectively. In this article, L_2 was 500-nH implemented by an air-core inductor.

More information about the components used in the prototype hardware is available in [18].

REFERENCES

[1] T. Suntio, "Methods to estimate load-transient response of buck converter under direct-duty-ratio and peak-current-mode control," *IEEE Trans. Power Electron.*, vol. 35, no. 6, pp. 6436–6446, Jun. 2020.

[2] S. Bari, Q. Li, and F. C. Lee, "A new fast adaptive on-time control for transient response improvement in constant on-time control," *IEEE Trans. Power Electron.*, vol. 33, no. 3, pp. 2680–2689, Mar. 2018.

[3] E. Meyer, Z. Zhang, and Y. F. Liu, "An optimal control method for buck converters using a practical capacitor charge balance technique," *IEEE Trans. Power Electron.*, vol. 23, no. 4, pp. 1802–1812, Jul. 2008.

[4] L. Corradini, A. Costabeber, P. Mattavelli, and S. Saggini, "Parameter-independent time-optimal digital control for point-of-load converters," *IEEE Trans. Power Electron.*, vol. 24, no. 10, pp. 2235–2248, Oct. 2009.

[5] E. Meyer, Z. Zhang, and Y. F. Liu, "Digital charge balance controller to improve the loading/unloading transient response of buck converter," *IEEE Trans. Power Electron.*, vol. 27, no. 3, pp. 1314–1326, Mar. 2012.

[6] L. Corradini, A. Babarzdeh, A. Bjeletić, and D. Maksimović, "Current-limited time-optimal response in digitally controlled DC-DC converters," *IEEE Trans. Power Electron.*, vol. 25, no. 11, pp. 2869–2880, Nov. 2010.

[7] G. Feng, E. Meyer, and Y. F. Liu, "A new digital control algorithm to achieve optimal dynamic performance in DC-to-DC converters," *IEEE Trans. Power Electron.*, vol. 22, no. 4, pp. 1489–1498, Jul. 2007.

[8] W. Lu, Y. Ruan, and H. H. C. Iu, "An auxiliary-parallel-inductor-based sequence switching control to improve the load transient response of buck converters," *IEEE Trans. Ind. Electron.*, vol. 66, no. 4, pp. 2776–2784, Apr. 2019.

[9] O. Kirshenboim, A. Cervera, and M. M. Peretz, "Improving loading and unloading transient response of a voltage regulator module using a load-side auxiliary gyrator circuit," *IEEE Trans. Power Electron.*, vol. 32, no. 3, pp. 1996–2007, Mar. 2017.

[10] Z. Shan, S. C. Tan, and C. K. Tse, "Transient mitigation of dc-dc converters for high output current slew rate applications," *IEEE Trans. Power Electron.*, vol. 28, no. 5, pp. 2377–2388, May 2013.

[11] S. Kapat, P. S. Shenoy, and P. T. Krein, "Near-null response to large-signal transients in an augmented buck converter: A geometric approach," *IEEE Trans. Power Electron.*, vol. 27, no. 7, pp. 3319–3329, Jul. 2012.

[12] E. Meyer, Z. Zhang, and Y. F. Liu, "Controlled auxiliary circuit to improve the unloading transient response of buck converters," *IEEE Trans. Power Electron.*, vol. 25, no. 4, pp. 806–819, Apr. 2010.

[13] L. Jia, Z. Hu, Y. F. Liu, and P. C. Sen, "Predictable auxiliary switching strategy to improve unloading transient response performance for DC–DC buck converter," *IEEE Trans. Ind. Appl.*, vol. 49, no. 2, pp. 931–941, Mar/Apr. 2013.

[14] A. Radić, Z. Lukić, A. Prodić, and R. H. Nie, "Minimum-deviation digital controller IC for DC-DC swith-mode power supplies," *IEEE Trans. Power Electron.*, vol. 28, no. 9, pp. 4281–4298, Sep. 2013.

[15] S. Saggini, M. Ghioni, and A. Geraci, "An innovative digital control architecture for low-voltage, high-current DC-DC converters with tight voltage regulation," *IEEE Trans. Power Electron.*, vol. 19, no. 1, pp. 210–218, Jan. 2004.

[16] Z. Shan, S. C. Tan, C. K. Tse, and J. Jatskevich, "Augmented buck converter design using resonant circuits for fast transient recovery," *IEEE Trans. Power Electron.*, vol. 31, no. 8, pp. 5666–5679, Aug. 2016.

[17] D. Kim, M. Hong, J. Baek, J. Lee, J. Shin, and J. W. Shin, "Soft-switching auxiliary current control for improving load transient response of buck converter," *IEEE Trans. Power Electron.*, vol. 36, no. 3, pp. 2488–2494, Mar. 2021.

[18] D. Kim, J. Baek, J. Lee, J. Shin, and J. W. Shin, "Implementation of soft-switching auxiliary current control for faster load transient response," *IEEE Access*, vol. 9, pp. 7092–7106, 2021.

[19] Y. W. Huang, T. H. Kuo, S. Y. Huang, and K. Y. Fang, "A four-phase buck converter with capacitor-current-sensor calibration for load-transient-response optimization that reduces undershoot/overshoot and shortens settling time to near their theoretical limits," *IEEE J. Solid-State Circuits*, vol. 53, no. 2, pp. 552–568, Feb. 2018.

[20] Z. Shan, C. K. Tse, and S. C. Tan, "Pre-energized auxiliary circuits for very fast transient loads: Coping with load-informed power management for computer loads," *IEEE Trans. Circuits Syst. I, Reg. Papers*, vol. 61, no. 2, pp. 637–648, Feb. 2014.

[21] T. Senanayake, and T. Ninomiya, "An improved topology of inductor switching DC-DC converter," *IEEE Trans. Ind. Electron.*, vol. 52, no. 3, pp. 869–878, Jun. 2005.

Dongwook Kim received the B.S. degree in electrical engineering from Dong-Eui University, Busan, South Korea, in 2019, and the M.S. degree in energy systems engineering in 2021 Chung-Ang University, Seoul, South Korea, where he is currently working toward the Ph.D. degree with the School of Energy Systems Engineering.

His research interests include dc–dc converter, power conversion system and its control, and power semiconductor packaging.

Jong-Won Shin (Member, IEEE) received the B.S. and Ph.D. degrees in electrical engineering from Seoul National University, Seoul, South Korea, in 2006 and 2013, respectively.

He was a Postdoctoral Researcher with Virginia Tech, Blacksburg, VA, USA, from 2013 to 2015, and a Senior Scientist with the Electronics Research Department, Toyota Research Institute of North America, Ann Arbor, MI, USA, from 2015 to 2018. Since 2018, he has been an Assistant Professor with Chung-Ang University, Seoul, South Korea. Since 2021, he has also been a Visiting Associate Professor with Nagoya University, Nagoya, Japan. His research interests include power conversion, energy management, and power semiconductor packaging.